

## Article

# Facile Construction of Intramolecular g-CN-PTCDA Donor-Acceptor System for Efficient CO<sub>2</sub> Photoreduction

Jiajia Wei <sup>1,†</sup> , Xing Chen <sup>2,†</sup>, Xitong Ren <sup>2</sup>, Shufang Tian <sup>1,\*</sup> and Feng Bai <sup>2,\*</sup> 

<sup>1</sup> Henan International Joint Laboratory of Medicinal Plants Utilization, College of Chemistry and Chemical Engineering, Henan University, Kaifeng 475004, China

<sup>2</sup> Key Laboratory for Special Functional Materials of Ministry of Education, National and Local Joint Engineering Research Center for High-Efficiency Display and Lighting Technology, Collaborative Innovation Center of Nano Functional Materials and Applications, School of Materials Science and Engineering, Henan University, Kaifeng 475004, China

\* Correspondence: tianshufang@henu.edu.cn (S.T.); baifengsun@126.com (F.B.)

† These authors contributed equally to this work.

**Abstract:** Due to the different electron affinity, the construction of a donor-acceptor (DA) system in the graphitic carbon nitride (g-CN) matrix is an attractive tactic to accelerate photo-induced electron-holes separation, and then further elevate its photocatalytic performance. In this work, perylene tetracarboxylic dianhydride (PTCDA) with magnificent electron affinity and excellent thermal stability was chosen to copolymerize with urea via facile one-pot thermal copolymerization to fabricate g-CN-PTCDA equipped with DA structures. The specific surface area of g-CN-PTCDA would be enlarged and the visible light absorption range would be broadened simultaneously when adopting this copolymerization strategy. A series of characterizations such as electron paramagnetic resonance (EPR), steady and transient photoluminescence spectra (PL), electrochemical impedance spectroscopy (EIS), and photocurrent tests combined with computational simulation confirmed the charge separation and transfer efficiency dramatically improved due to the DA structures construction. When 0.25% wt PTCDA was introduced, the CO evolution rate was nearly 23 times than that of pristine g-CN. The CO evolution rate could reach up to 87.2  $\mu\text{mol g}^{-1} \text{h}^{-1}$  when certain  $\text{Co}^{2+}$  was added as co-catalytic centers. Meanwhile, g-CN-1 mg PTCDA-Co exhibited excellent long-term stability and recyclability as a heterogeneous photocatalyst. This research may shed light on designing more effective DA structures for solar-to-energy conversion by CO<sub>2</sub> reduction.

**Keywords:** donor-acceptor; graphitic carbon nitride; PTCDA; photocatalysis; CO<sub>2</sub> reduction



**Citation:** Wei, J.; Chen, X.; Ren, X.; Tian, S.; Bai, F. Facile Construction of Intramolecular g-CN-PTCDA Donor-Acceptor System for Efficient CO<sub>2</sub> Photoreduction. *Catalysts* **2023**, *13*, 600. <https://doi.org/10.3390/catal13030600>

Academic Editors: Weilong Shi, Feng Guo, Xue Lin and Yuanzhi Hong

Received: 13 February 2023

Revised: 9 March 2023

Accepted: 14 March 2023

Published: 16 March 2023



**Copyright:** © 2023 by the authors. Licensee MDPI, Basel, Switzerland. This article is an open access article distributed under the terms and conditions of the Creative Commons Attribution (CC BY) license (<https://creativecommons.org/licenses/by/4.0/>).

## 1. Introduction

CO<sub>2</sub> plays a vital role in the global carbon cycle. The earth's environment and ecosystem have been greatly challenged in the past decades due to excessive CO<sub>2</sub> being emitted into the atmosphere. Numerous attempts have been made to get around this challenge, as the photocatalytic reduction of CO<sub>2</sub> to value-added chemicals under visible light is one of the effective strategies used to fulfill the resource utilization of CO<sub>2</sub> [1–5]. However, the high stability of CO<sub>2</sub> molecules and the varied reduction used products during the reduction process limit its practical application. To this end, a common strategy to elevate the catalytic performances is to regulate and optimize the structures and properties of the photocatalysts.

g-CN, as a metal-free organic polymeric semiconductor, possesses a suitable bandgap and responses to visible light. It is gifted with excellent thermal and chemical stability and has been extensively explored in photocatalysis fields [6–10]. Nevertheless, the rapid recombination of photo-induced charge carriers, the limited visible light harvesting ability and specific surface area hinder its catalytic performance on CO<sub>2</sub> reduction. To promote

the exciton dissociation efficiency, intramolecular DA structures based on g-CN via bottom-up copolymerization have been established [11–16] over the past few years and have exhibited optimized photocatalytic activity. The different electron affinity of the donor and acceptor units would induce electrons to migrate from donor to acceptor parts and further promote charge carriers to disjoin into free electrons and holes. While there are still some aspects that should be noted, the first is that the selected electron-withdraw molecules as co-monomers should maintain extremely high thermal stability. The second is that the picked molecules ought to bear the functional groups that can be covalently imbedded into the skeleton of g-CN during the thermal polymerization. The last is that the properties of g-CN, such as specific surface area or light-harvesting capacity, may also be modulated during copolymerization process.

Based on the above restraints, PTCDA is the optimal choice to fulfill DA structures construction due to its magnificent electron affinity, exceptional thermal stability, and bearing dianhydride functional groups that can react with the amino groups of urea to form diimide covalent bonds. Furthermore, the resultant fragment 3, 4, 9, 10-perylenetetracarboxylic diimide (PTI) as an n-type organic semiconductor owns extraordinary light absorption in the visible region and is widely applied in photocatalytic reactions owing to its more positive valence band [17–21]. A series of Z-scheme PTCDA-C<sub>3</sub>N<sub>4</sub> heterostructure photocatalysts have been fabricated previously via imidization reaction and have exhibited remarkable photocatalytic performance in various photocatalytic applications [22–26]. The fact is that the amount of the amine group suspended on the edge of g-CN nanosheets is limited and PTCDA is prone to self-aggregate due to its planar  $\pi$ -conjugated macrocycle structure. Furthermore, the property of a g-CN-like specific surface area can hardly be tuned by traditional post-synthetic modification or other noncovalent composites methods. Nevertheless, it could possibly be accomplished by adopting the copolymerization method because the introduction of a co-monomer may alter the course of the polymerization process so as to regulate the properties of g-CN.

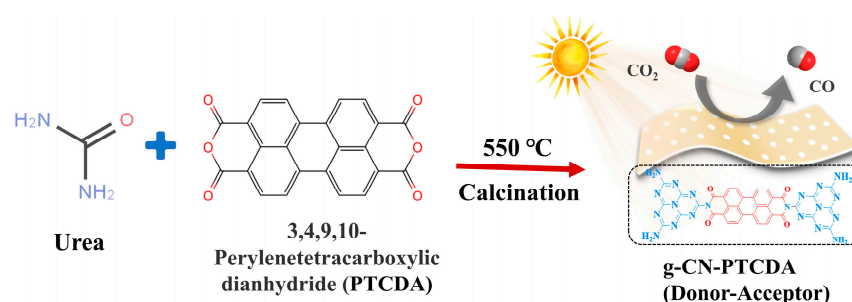
Herein, PTCDA is selected as a co-monomer to bottom-up copolymerize with urea to construct intramolecular DA structures based on g-CN, in which PTCDA served as the acceptor units to capture and store electrons as catalytic active centers due to its distinguished electron affinity, while g-CN composed of heptazine fragments acted as donor units when irradiated under visible light. The obtained g-CN-PTCDA, including DA segments, can not only speed up the photo-induced exciton dissociation but also shorten the migration distances of the electrons or holes to its surface, which results from the expanded specific surface area and the diminished thickness of the g-CN-PTCDA nanosheets. The visible light absorption region was also broadened at the same time due to the photo-sensitiveness of PTCDA. The g-CN-PTCDA with DA structures exhibited a dramatically advanced photocatalytic CO<sub>2</sub> reduction with a maximum CO evolution rate of 5.25  $\mu\text{mol g}^{-1} \text{h}^{-1}$ , which was nearly 23-folds that of the unmodified g-CN. This work offers a new concept for the fabrication of all organic photocatalysts for CO<sub>2</sub> reduction, in which PTCDA can function as a catalytic center due to its ability to capture and accumulate electrons.

## 2. Results and Discussion

All photocatalyst g-CN-*x* mg PTCDA possess DA structures that can be successfully fabricated via facile one-pot thermal co-polymerization [27,28] by employing a different mass ratio of urea and PTCDA as co-monomers, as shown in Scheme 1.

Firstly, the thermal stability of PTCDA was checked by TG and FT-IR analysis (Figure S1a,b, Supplementary Materials). PTCDA maintained 96.7% of its original mass when the temperature increased to 550 °C. The FT-IR spectrum showed that the typical peaks of PTCDA remained unchanged before and after calcination under the same copolymerization condition, indicating the exceptional high thermal stability of PTCDA. The color of g-CN-*x* mg PTCDA turned light gray from the yellow powder of the pristine g-CN, it then gradually deepened to dark green along with the increasing amount of PTCDA, and

finally presented as a dark purple when the amount of PTCDA increased to 1 g (Figure S2, Supplementary Materials).



**Scheme 1.** Schematic illustration of the preparation of the g-CN-PTCDA composite photocatalyst with DA structure using the one pot thermal copolymerization method.

The morphologies of g-CN and the obtained g-CN-*x* mg PTCDA were investigated by SEM and TEM images. As can be seen, g-CN-1 mg PTCDA retained the fluffy stacking nanosheets (Figure 1b) as g-CN (Figure 1a,d), except that a more abundant mesoporous structure formed, which is in accordance with the semitransparent porous nanosheets with rough edges obtained by TEM characterization (Figure 1e). Some regular nano-rods formed and piled up on the surface of the g-CN nanosheets (Figure 1c,f) when the load of PTCDA increased to 1 g, suggesting that the self-assembly of the excessive unreacted of PTCDA formed via  $\pi$ - $\pi$  stacking. TEM mapping was also employed to analyze the elemental distribution of the sample (Figure 1g). Carbon, nitrogen, and oxygen (originated from the C=O of PTCDA) elements are evenly distributed in the selected region, which demonstrates the covalent connection of PTCDA and g-CN and that the DA structures were successfully constructed.

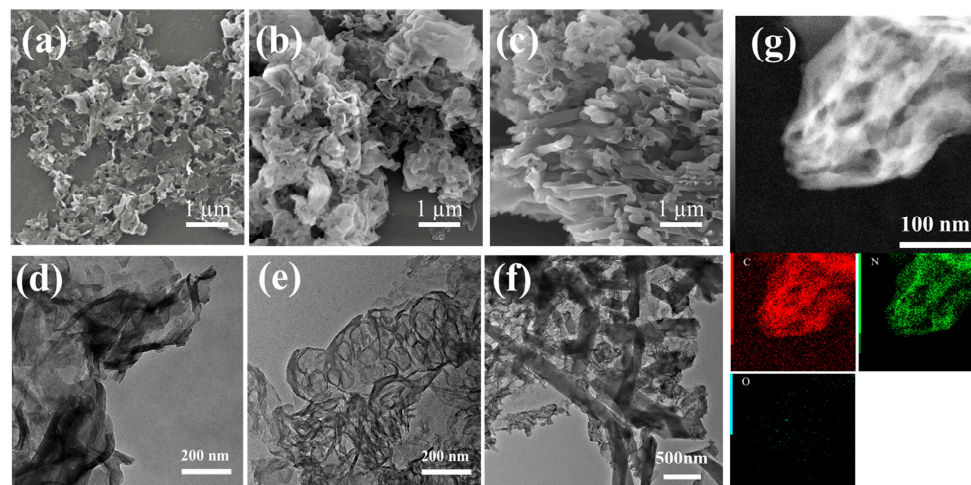


**Figure 1.** SEM images of the g-CN (a), g-CN-1 mg PTCDA (b), and g-CN-1g PTCDA (c). TEM images of the g-CN (d), g-CN-1 mg PTCDA (e), and g-CN-1g PTCDA (f) and the corresponding elemental mappings of the enlarged area of g-CN-1mg PTCDA (g).

The specific surface area and mesopores distribution were studied by  $\text{N}_2$  adsorption-desorption measurements. As shown in Figure 2a, g-CN-1mg-PTCDA exhibited an obviously enhanced adsorption capacity and the specific surface area increased to  $97\text{ m}^2\text{ g}^{-1}$  compared with  $36\text{ m}^2\text{ g}^{-1}$  of g-CN. The isotherm for g-CN-1mg PTCDA presented an obvious H1 type hysteresis loop at relative pressure  $p/p_0 > 0.8$ , indicating the slit-type holes formed by nanosheets stacking [29,30]. The pore volume of g-CN-1 mg PTCDA was also apparently promoted and the pore size distribution shows that the pore size was concentrated at 2.6 and 29 nm (Figure 2b). This enlarged specific surface area can hardly be fulfilled through traditional post-synthetic modification.

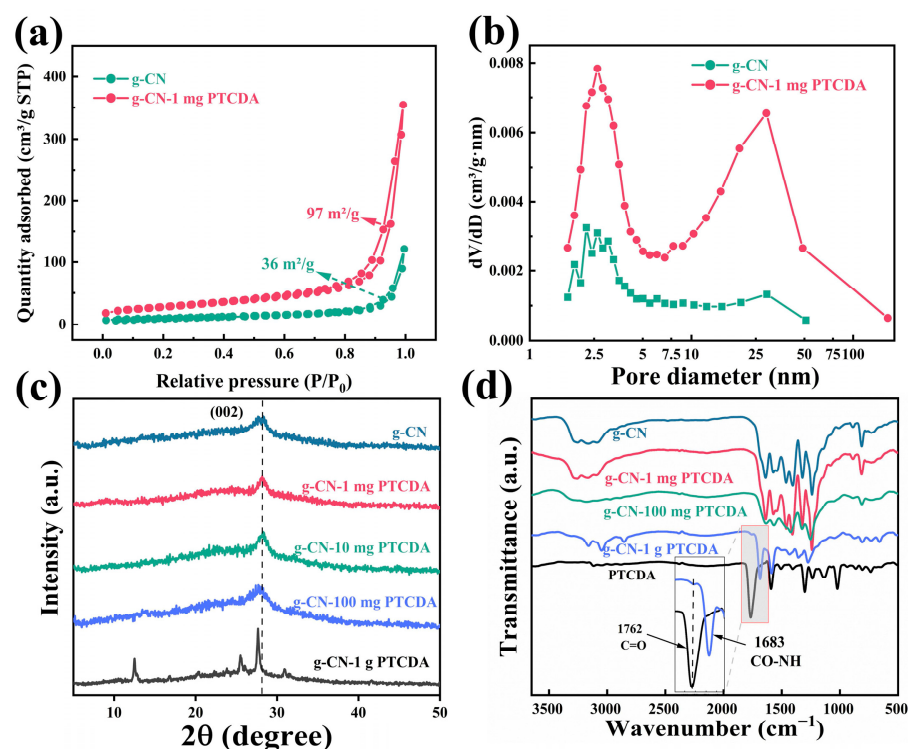


**Figure 2.** N<sub>2</sub> adsorption-desorption isotherms (a) and the corresponding pore size distribution curves (b) of g-CN and g-CN-1 mg PTCDA. XRD patterns (c), and FT-IR spectra (d) of the samples of g-CN and g-CN-*x* mg PTCDA (*x* = 1, 10, 100, 1000).

XRD was used to study the crystal structure of the samples. As shown in Figure 2c, g-CN-*x* mg PTCDA (*x* = 1, 10, 100) showed two distinct diffraction peaks at around 13° and 27° which correspond to the (100) and (002) crystal planes as g-CN [31]. The (100) crystal plane is ascribed to the repeating motif of tri-*s*-triazine in-plane and the (002) plane is from the stacking of aromatic systems of the interlayer, which indicates that the crystal structures are well retained after the introduction of PTCDA. When the amount of PTCDA is raised to 1 g, the XRD pattern was clearly different from g-CN but similar to that of the PTCDA powder, and the diffraction peaks belong to the  $\pi$ - $\pi$  stacking of excessive unreacted PTCDA.

FT-IR spectra were recorded to index the chemical structure and the covalent interactions between PTCDA and g-CN (Figure 2d). g-CN-*x* mg PTCDA (*x* = 1, 100) exhibited approximate characteristic absorption bands as g-CN, the typical peak at 810, 1200–1600, and 3000–3500 cm<sup>-1</sup> are attributed to the bending vibration of the triazine ring, the stretching vibrations of the aromatic heptazine heterocycles, and the NH<sub>2</sub> groups located on the edges of the g-CN nanosheets, respectively. When the amount of PTCDA was raised up to 1 g, it can be clearly seen that the typical peak at 1742 cm<sup>-1</sup> arising from the C=O in the anhydride groups of PTCDA disappeared, and the peak at 1683 cm<sup>-1</sup> is newly generated, which can be ascribed to the stretching vibrations of the C=O in the diimide group. The result provides solid evidence that the DA structures successfully constructed between PTCDA and g-CN via covalent bonds.

The surface chemical states of C, N, O and the interfacial interaction were studied by XPS. Figure 3a is the XPS survey spectra of g-CN and g-CN-PTCDA, from which we can see that the peaks of O 1s emerged with the introduction of PTCDA and the intensity increased when the PTCDA content increased. A high resolution of the C 1s spectra is presented in Figure 3b. For pure g-CN, the binding energy of C 1s is dominantly situated at 287.8 eV, which corresponds to the sp<sup>2</sup>-hybridized C from N-C=N. The C 1s spectra of g-CN-*x* mg PTCDA (*x* = 1, 10) are deconvoluted into three peaks, except for the sp<sup>2</sup>-hybridized N-C=N, in which the peaks at 286.07 and 284.81 eV are attributed to sp<sup>2</sup>-hybridized C=O and C=C

coming from PTCDA and the peak areas increase along with the added PTCDA weight percentage [22,32]. Figure 3c presents the N 1s binding energies of g-CN. The divided three peaks at 398.59, 400.31, and 401.36 eV of g-CN belong to the  $sp^2$ -hybridized N involved in the triazine rings, the bridging  $sp^3$ -hybridized N in the melem motif center, and the amino group  $-NH_x$ , respectively [33–35]. The peaks of  $sp^2$ -hybridized N (C-N=C) in g-CN- $x$  mg PTCDA ( $x = 1, 10$ ) both shift about 0.27 eV to a higher binding energy (398.86 eV) in contrast with g-CN, illustrating when the strong electron-withdrawing group PTCDA is introduced, the electron cloud density in heptazine ring decreased, demonstrating the efficient DA structures established in the matrix of g-CN-PTCDA. In addition, the mass ratio of C/N obtained from XPS are showed in Table S1, and the value of the C/N ratio increased along with the content of PTCDA raised. The binding energy of O 1s that originated from O=C (Figure 3d) was 531.9 eV and the intensity of the peaks also increased with the improved content of PTCDA.

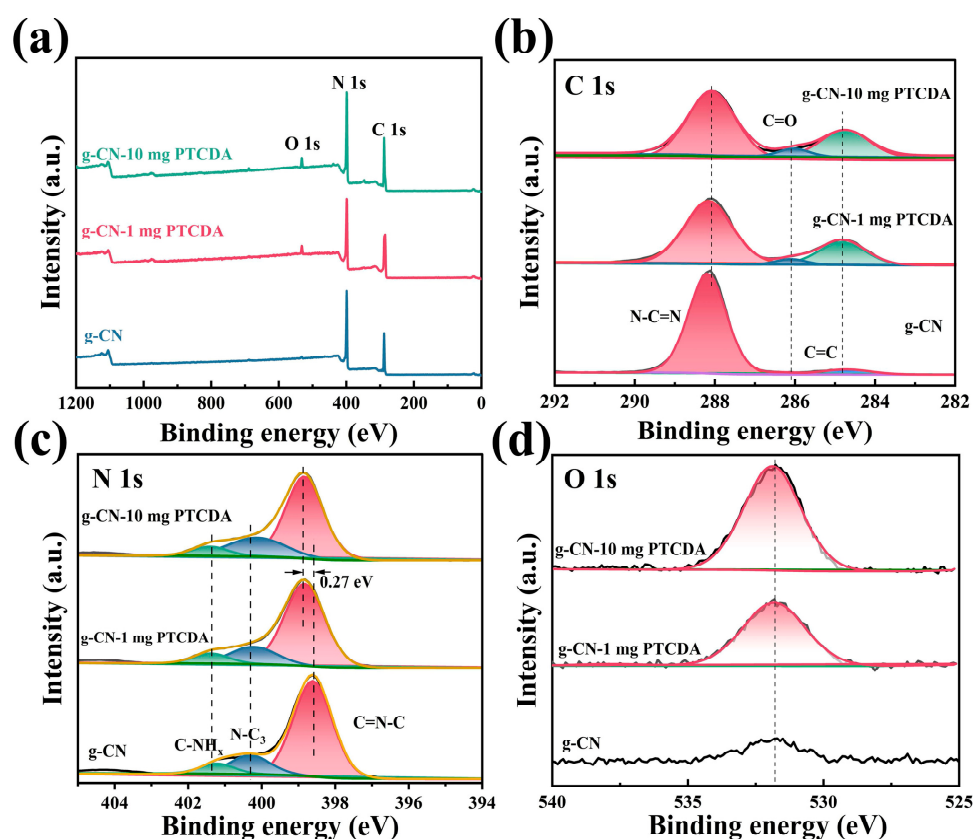


**Figure 3.** XPS-survey (a), high-resolution of C 1s (b), N 1s spectra (c), and O 1s spectra (d) of the samples of g-CN, g-CN-1 mg PTCDA, and g-CN-10 mg-PTCDA.

UV-vis DRS spectra were conducted to study the optical absorption properties of the g-CN and g-CN- $x$  mg PTCDA. As shown in Figure 4a, the absorption band edges of g-CN- $x$  mg PTCDA ( $x = 1, 10, 100, 1000$ ) are gradually red-shifted, and the visible-light response range steadily expanded to the full spectra region accompanying the amount of PTCDA raised, fully indicating that PTCDA covalently connected with g-CN via imide bonds. The corresponding band gaps of g-CN- $x$  mg PTCDA ( $x = 1, 10$ ) are respectively calculated as 2.51, 2.44 eV based on the Tauc plots method (Figure 4b), and they are narrower than the 2.75 eV of g-CN, which can be explained by the  $\pi$  electrons being delocalized along the expanded conjugation system between PTCDA and g-CN.P

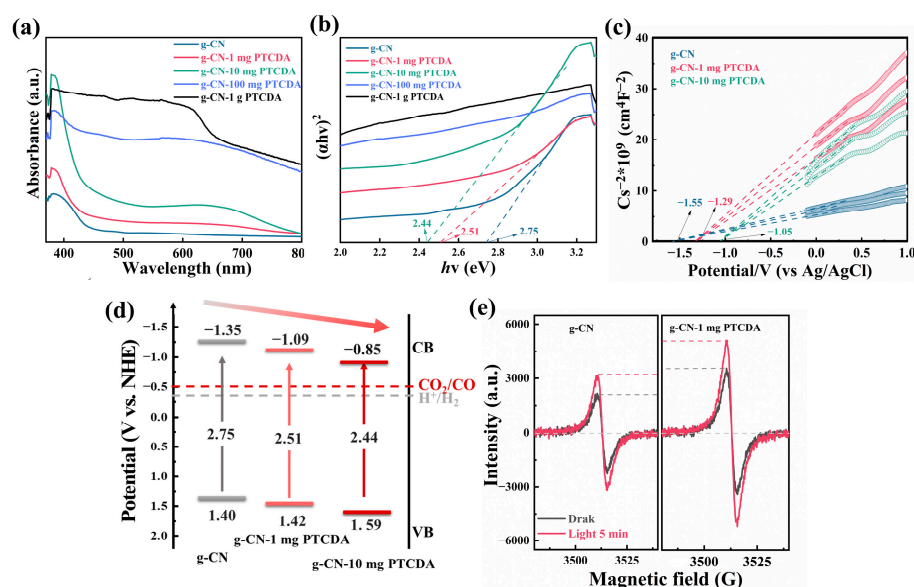


**Figure 4.** Optical absorption and band positions of g-CN, g-CN-1 mg PTCDA, and g-CN-10 mg PTCDA samples. UV-vis DRS spectra (a) and the corresponding Tauc plots (b), Mott–Schottky plots (c), energy diagrams of the band structure (d). EPR spectra of the g-CN and g-CN-1 mg PTCDA at room temperature (e).

The conduction band energy was obtained by testing the Mott–Schottky curve, in which the straight-line part of the curve is extrapolated to the abscissa axis, and the intersection point is the flat-band potential. Generally, for n-type semiconductors, the position of the conduction band bottom is consistent with the flat band potential, which can be considered as the position of the conduction band bottom. From Figure 4c, we can learn that g-CN-PTCDA is a typical n-type semiconductor due to the positive slope. The flat-band potential of g-CN, g-CN-1 mg PTCDA, and g-CN-10 mg PTCDA are located at  $-1.55$ ,  $-1.29$ , and  $-1.05$  eV (vs. Ag/AgCl), which could be converted to  $-1.35$ ,  $-1.09$ , and  $-0.85$  V (vs. NHE), respectively and are more negative than that of the required potential of reducing  $\text{CO}_2$  to  $\text{CO}$  ( $-0.53$  V). Regarding the combination with the band gap values determined in Figure 4b, the CB potentials of g-CN, g-CN-1 mg PTCDA, and g-CN-10 mg PTCDA are calculated to be  $1.40$ ,  $1.42$ , and  $1.59$  V, respectively, as shown in Figure 4d.

The electronic structure of the g-CN and g-CN-PTCDA were explored by EPR measurements. As can be seen in Figure 4d, g-CN-1 mg PTCDA showed dramatically improved signals of the Lorentzian line with a g value of  $2.0034$  than that of g-CN, which originated from the unpaired electrons in the conduction bands of g-CN-1 mg PTCDA [36]. It means that a high concentration of unpaired electrons generated due to the DA structures. Besides, the charge separation efficiency of g-CN-1 mg PTCDA was more notable than that of g-CN under illumination conditions, which is conducive to promote the photocatalytic  $\text{CO}_2$  reduction performance.

### 3. Photocatalytic Performance

The photocatalytic performances of the prepared g-CN-PTCDA were assessed by  $\text{CO}_2$  reduction. Considering that the gas  $\text{CO}_2$  has higher solubility in the organic solvent, and in order to suppress the proton reduction as a competition reaction,  $\text{CH}_3\text{CN}$  was chosen as the reaction solvent. TEOA was selected as the sacrificial agent to capture the unreacted photo-induced holes because it was extensively used and displayed the highest photocatalytic  $\text{CO}_2$  reduction activity compared with other sacrificial agents [37–39], and the volume ratio of  $\text{CH}_3\text{CN}/\text{TEOA}$  was 4:1. The photocatalytic reaction was carried out under 5 W LED lamp ( $\lambda > 420$  nm) irradiation and the reaction temperature was set at  $6^\circ\text{C}$  with circulating condensed water. The control experiments showed that there was negligible  $\text{CO}$  or  $\text{CH}_4$

detected as the reduction products without one of the factors including the irradiation, the photocatalyst, TEOA, or using  $N_2$  instead of  $CO_2$ .

As presented in Figure 5a, the experiment results showed that CO was the main reduction product along with some amount of  $H_2$  generated as the byproduct, and the  $H_2$  was mainly from the partial degradation of TEOA. The CO evolution rate was  $0.23 \mu\text{mol g}^{-1} \text{h}^{-1}$  when using unmodified g-CN as the photocatalyst, along with a  $H_2$  generation rate of  $0.43 \mu\text{mol g}^{-1} \text{h}^{-1}$  and the selectivity was 35% over proton reduction. When a certain amount of PTCDA was introduced into the skeleton of g-CN and the intramolecular DA system was constructed, the photocatalytic activity remarkably improved. The CO evolution rate can reach up to  $5.25 \mu\text{mol g}^{-1} \text{h}^{-1}$  when the loading content of PTCDA was 1 mg, which is nearly 23-folds that of pristine g-CN. The  $H_2$  generation rate was  $1.14 \mu\text{mol g}^{-1} \text{h}^{-1}$  and the selectivity improved to 82%. The CO evolution rate began to descend with the continuous increment of PTCDA, as introducing too much PTCDA would destroy the conjugate structural integrity of g-CN and further weaken its light-harvesting ability.

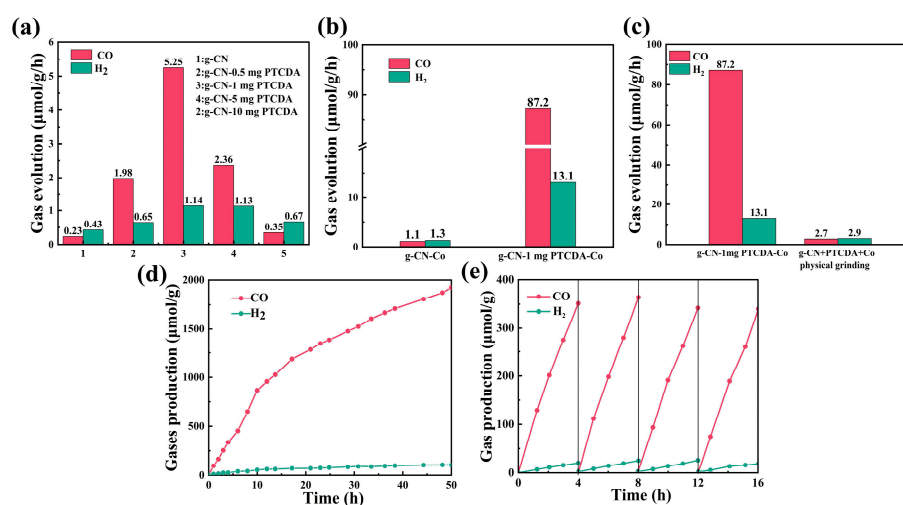


**Figure 5.** The effects of different PTCDA contents on the evolution of CO and  $H_2$  (a), g-CN-Co and g-CN-1 mg PTCDA-Co gases production rate (b), comparison of CO and  $H_2$  evolution rates of the covalent bond connection and physical mixing of g-CN and PTCDA (c),  $CO_2$  reduction stability of g-CN-1 mg PTCDA-Co under 50 h light condition (d), the yields of CO and  $H_2$  under the catalytic action of g-CN-1 mg PTCDA-Co over four continuous cycles and each cycle lasted 4 h (e).

Afterward, the photocatalyst g-CN-1 mg PTCDA-Co was fabricated by hydrothermal synthesis, where  $Co^{2+}$  was introduced, acting as the co-catalytic center, and the CO evolution rate dramatically increased to  $87.2 \mu\text{mol g}^{-1} \text{h}^{-1}$ . The  $H_2$  generation rate was  $13.1 \mu\text{mol g}^{-1} \text{h}^{-1}$  and the selectivity was 87%, which was more than 79-folds that of g-CN-Co (Figure 5b). This indicates that the electrons separated and accumulated on the PTCDA unit can quickly transfer to the catalytic active sites  $Co^{2+}$ , thus the catalytic performance dramatically enhanced. From Table S2, we can learn that the photocatalysts g-CN-1 mg PTCDA and g-CN-1 mg PTCDA-Co performed satisfactory photocatalytic  $CO_2$  reduction performance.

The control experiment was also conducted to investigate the cause for the elevated catalytic activity (Figure 5c). The PTCDA compounded with g-CN through physical grinding and the CO evolution rate exhibited certain enhancement ( $2.7 \mu\text{mol g}^{-1} \text{h}^{-1}$ ) with a selectivity of 48% over  $H_2$ , implying that the covalent connection between PTCDA and g-CN is indispensable.

The stability and reusability of the g-CN-1 mg PTCDA-Co were further evaluated. As shown in Figure 5d, the CO evolution rate maintained a near linear growth of up to 50 h with the average rate of  $38.4 \mu\text{mol g}^{-1} \text{h}^{-1}$ , displaying the long-term robustness of the photocatalyst. As for the reusability, in the 16 h sequent reaction, that is, 4 consecutive cycles

where each cycle lasts 4 h, no noticeable declination was observed (Figure 5e), signifying the excellent recyclability of g-CN-PTCDA-Co as a heterogeneous photocatalyst.

The properties of the recovered g-CN-1 mg PTCDA-Co after the long-term catalytic process were also studied by FT-IR, XRD, and TEM (Figure S3, Supplementary Materials). The characterization showed that the chemical and crystal structure of g-CN-PTCDA-Co remained unchanged and the morphology also remained intact, suggesting its fine and lasting photo stability.

#### 4. Structure–Activity Relationship and Mechanism Discussion

A combination of the photocatalytic CO<sub>2</sub> reduction performance and the characterizations of g-CN-PTCDA, the enhanced photocatalytic activity, and the selectivity, can be ascribed to the following factors.

The construction of the intramolecular DA system plays a functional role [40–43]. As we know, the separation, migration, and transmission efficiency of photo-generated electron-holes are the key elements that affect the photocatalytic performance. The different electrons binding ability between PTCDA and g-CN boost the electrons transferred from g-CN to PTCDA and the separation efficiency of the charge carriers is greatly accelerated, which can be verified by the fluorescence and electrochemical tests.

Steady-state PL analysis is generally recognized as the technique used to characterize the recombination of photo-induced electron-holes, that is, the higher the peak intensity, the more recombinations of the photogenerated electrons and holes occur. As can be seen in Figure 6a, the PL intensity of g-CN-1 mg PTCDA decreased sharply in comparison with that of g-CN, which exhibited a strong PL emission peak excited at 365 nm at room temperature, fully illustrating that the recombination of the photogenerated electron-holes has been greatly inhibited. In addition, time resolved PL spectra were also performed to evaluate the dynamic photoinduced electron behaviors. In Figure 6b, the g-CN-1 mg PTCDA exhibits a shorter average fluorescence lifetime (4.29 ns) than that of g-CN (4.97 ns), indicating a more efficient non-radiative decay pathway between PTCDA and g-CN. The electron transfer rate ( $k_{ET}$ ) calculated using the equation [44,45] was  $3.2 \times 10^7 \text{ s}^{-1}$  (Table S3) between g-CN and PTCDA, illustrating the fast spatial charge separation efficiency through the intramolecular DA system.

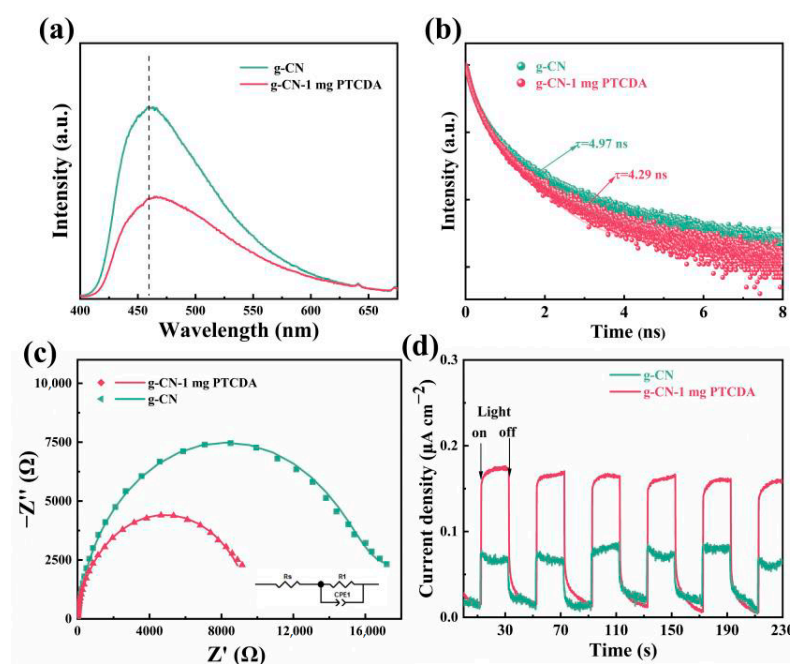


**Figure 6.** Steady-state PL spectra (a), time-resolution PL decay spectroscopy (b), Nyquist plots with the inset of the simulated circuit (c), photocurrent response (d) of the samples of g-CN and g-CN-1 mg PTCDA.

As for the EIS, a smaller arc radius commonly means lower electron-transfer resistance. In Figure 6c, the arc radius of g-CN-1 mg PTCDA is much smaller than that of g-CN and the fitting results are present in Table S4, implying the interfacial electrons' fast mobility of g-CN-1 mg PTCDA due to the lower resistance.

In addition, g-CN-1 mg PTCDA exhibited dramatically enhanced and steady photocurrent responses compared to g-CN, without significant decay after six repetitive cycles (Figure 6d), demonstrating that the DA system constructed between PTCDA and g-CN was more conducive to charge separation and transfer than g-CN, which is in accordance with the results of the PL and EIS analysis.

Furthermore, the electrostatic potential (ESP) surface distribution of the g-CN-PTCDA was built with a GaussView program. The method employed to optimize the structure model is B3LYP/6-31g. The computed result affords a feasible electron transfer route during this DA system. As can be seen in Figure 7, in this ESP map, the red color stands for the electrons affluent region while the blue color means the electron deficiency zone. As for the sample g-CN-PTCDA, the electrons migrate from g-CN to the oxygen atom of PTCDA, which can not only accelerate the separation of the electron-hole pairs, but PTCDA can also be regarded as an electron reservoir to drive the CO<sub>2</sub> reduction.

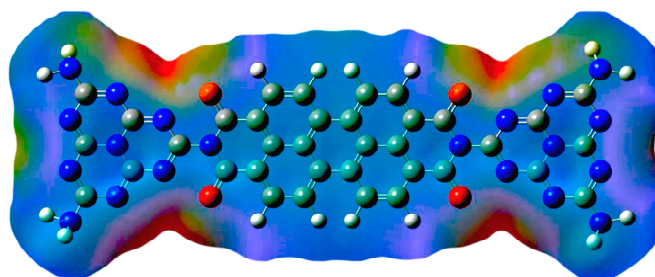


Figure 7. Optimized ESP surface distribution of the g-CN-PTCDA model.

Based on above analysis, a presumable mechanism using g-CN-1 mg PTCDA for CO<sub>2</sub> photoreduction is proposed (Figure 8). The photosensitizer g-CN absorbs visible light and the electrons excited from the valance band of g-CN to the LUMO level of the PTCDA, which is caused by the different electron affinities of PTCDA and g-CN. Then, electrons are accumulated on the PTCDA units while the holes are left on the g-CN parts. The intramolecular DA structures promote electrons migration and inhibit the electron-hole pairs recombination. Simultaneously, the enlarged specific surface area of g-CN-1 mg PTCDA facilitates more adsorption of CO<sub>2</sub> molecules. The process of the proton-coupled two electrons reduction is used to reduce CO<sub>2</sub> to CO ( $\text{CO}_2 + 2\text{H}^+ + 2\text{e}^- \rightarrow \text{CO} + \text{H}_2\text{O}$ ,  $-0.53\text{ V}$ ). Meanwhile, TEOA is added in the reaction system as a sacrificial electron donor to consume the unreacted holes to fasten the separation of electron-hole pairs and promote the CO<sub>2</sub> reduction performance.

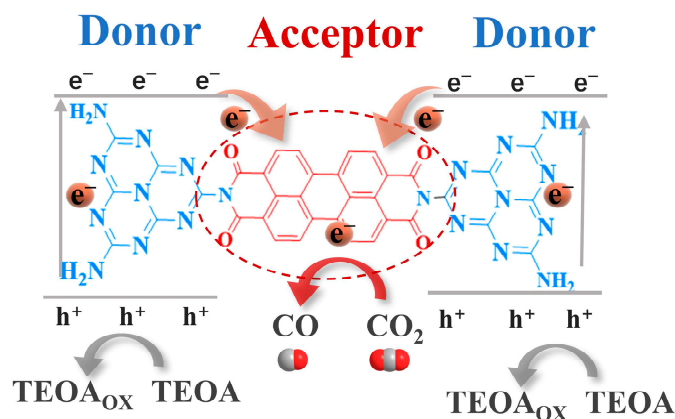


Figure 8. The mechanism of g-CN-1 mg PTCDA as a photocatalyst for CO<sub>2</sub> reduction is proposed.

## 5. Experimental Section

### 5.1. Reagents and Materials

Urea was obtained from J&K Scientific (Beijing, China). Acetonitrile ( $\text{CH}_3\text{CN}$ ), triethanolamine (TEOA), and PTCDA were purchased from Aladdin (Shanghai, China).  $\text{CoCl}_2 \cdot 6\text{H}_2\text{O}$  was provided by Maikelin (Fairfield, CT, USA).  $\text{Na}_2\text{SO}_4$  was obtained from Kermel (Tianjin, China). All the chemical reagents were used as received without further treatment. Ultra-pure water used in the experiment was prepared by the instrument THM-50131954 (Thermo Scientific, Waltham, MA, USA).

### 5.2. Preparation of Catalysts

#### 5.2.1. Preparation of g-CN

In detail, 20 g urea was placed in a crucible, covered with tin foil and heated in an ambient atmosphere to  $550\text{ }^\circ\text{C}$  in a muffle furnace at a heating rate of  $3\text{ }^\circ\text{C min}^{-1}$  and then kept at  $550\text{ }^\circ\text{C}$  for 2 h. The pale-yellow loose powder sample was obtained by natural cooling to room temperature.

#### 5.2.2. Preparation of g-CN- $x$ mg PTCDA

The samples with DA structures were synthesized by a facile one-pot thermal copolymerization method. In detail, 20 g urea and  $x$  mg PTCDA ( $x = 0.5, 1, 10, 100, 1000$ ) were weighted and then fully grinded and mixed. The mixture was transferred to a crucible with a tin foil cover and heated to  $550\text{ }^\circ\text{C}$  for 2 h at a heating rate of  $3\text{ }^\circ\text{C min}^{-1}$  in a muffle furnace. When the reaction cooled to room temperature, the obtained samples were named g-CN- $x$  mg PTCDA, where  $x$  stands for the initial mass of added PTCDA.

#### 5.2.3. Preparation of g-CN-Co and g-CN-1 mg PTCDA-Co

The samples were prepared by a typical hydrothermal method. At first, g-CN (50 mg) or g-CN-1 mg PTCDA (50 mg) were uniformly dispersed in 10 mL deionized water and then 2.4 mg  $\text{CoCl}_2 \cdot 6\text{H}_2\text{O}$  was added and stirred for 30 min to ensure sufficient dissolution. The mixture was then transferred to the autoclave for treatment at  $120\text{ }^\circ\text{C}$  for 12 h. When cooled to room temperature, the precipitate was centrifuged and washed successively with ultrapure water twice and EtOH once, and then dried at  $80\text{ }^\circ\text{C}$  for 12 h. The resultant samples were denoted as g-CN-Co or g-CN-1 mg PTCDA-Co.

### 5.3. Physicochemical Characterization

The morphologies of the samples were investigated by scanning electron microscopy (SEM, Nova NanoSEM 450, FEI, Hillsboro, OR, USA) and transmission electron microscope (TEM, JEM-2100F, Kitakyushu, Japan). Powder X-ray diffraction (XRD) was carried out on an X-ray diffractometer (Rigaku Dmax-2500, Tokyo, Japan) with a Cu K source. FT-IR spectra were recorded by VERTEX 70 spectrometer (Bruker, Billerica, MA, USA) in the range of  $4000$  to  $400\text{ cm}^{-1}$ . The samples were prepared by mixing the sample with FT-IR-grade KBr and the KBr was used as the reference. X-ray photoelectron spectroscopy (XPS) measurements were conducted on the XPS instrument (ESCALAB 250XI, Thermo, Waltham, MA, USA), the excitation source for Al target  $\text{K}\alpha$  rays ( $1486.6\text{ eV}$ ). Inductively coupled plasma atomic emission spectrometer (ICP) was performed with an Agilent 7800 ICP-MS. The UV-vis absorption was measured with UV-vis diffuse reflectance (UV-vis DRS, PerkinElmer Lambda 950, Waltham, MA, USA) using  $\text{BaSO}_4$  as the reflectance standard reference. Steady and transient PL spectra were carried out using a fluorescence spectrometer (FLS 980, Edinburgh, UK) (exciting samples by  $365\text{ nm}$  photons).

### 5.4. Photoelectrochemical Measurements

Photoelectrochemical measurements were monitored by a CHI 760E electrochemical workstation with a conventional three-electrode cell. The measurement processes were performed in a  $0.2\text{ M Na}_2\text{SO}_4$  aqueous solution. Ag/AgCl electrode and Pt plate were used as the reference electrode and counter-electrode. The working electrodes were fabricated

by using an as-prepared catalyst coated on indium tin oxide (ITO) glass. The photocurrent as a function of time was recorded as the light was switched on and off every 20 s. The electrochemical impedance was also recorded in the range of 0.1 MHz–0.1 Hz. Mott-Schottky plots were recorded at frequencies of 1000, 1100, and 1200 Hz. N<sub>2</sub> was blown into the electrolyte for 20 min before any electrochemical measurement was made.

### 5.5. Photocatalytic CO<sub>2</sub> Reduction

In a typical photocatalytic reaction, 5 mg photocatalyst was dispersed in 4 mL CH<sub>3</sub>CN in 50 mL quartz test bottle, along with 1 mL TEOA added as the electron sacrificial agent to trap the unreacted photo-induced holes. Before photocatalytic testing, the whole reaction system was evacuated and then bubbled with CO<sub>2</sub> (99%, Sigma-Aldrich, St. Louis, MO, USA) three times. The light source was a 5 W LED lamp (PCX-50C, Perfectlight, Beijing, China) with  $\lambda > 420$  nm cutoff filter. The reaction temperature was set at 6 °C with circulating condensed water.

The gas products, including CO and H<sub>2</sub>, were measured by gas chromatography (GC9790 II, Zhejiang Fuli, Wenling, China) equipped with a thermal conductivity detector (TCD) and a flame ionization detector (FID). In the cycle experiment, 5 mg g-CN-1 mg PTCDA-Co was used for photocatalysis, and the catalyst was recycled, washed, and dried in turn when each cycle ended.

## 6. Conclusions

The intramolecular DA system, g-CN-PTCDA, has been successfully constructed through copolymerization, employing PTCDA and urea as the starting material to elevate the photocatalytic performance towards CO<sub>2</sub> reduction. This strategy can not only enlarge the specific surface area of pristine g-CN and extend the visible light absorption range, but the constructed D-A structure can also boost the electrons transmission and suppress the recombination of the photo-induced electron-holes. The CO<sub>2</sub> reduction activity was 23-folds that of pristine g-CN and the CO evolution rate can reach up to 87.2  $\mu\text{mol g}^{-1} \text{h}^{-1}$  when Co<sup>2+</sup> is added as co-catalytic centers. The structure–activity relationship and the possible mechanism are also explored.

**Supplementary Materials:** The following supporting information can be downloaded at: <https://www.mdpi.com/article/10.3390/catal13030600/s1>, Figure S1. TG (a), and the FT-IR spectra (b) of PTCDA before and after calcination under copolymerization conditions, Figure S2. The photographic images of g-CN (a), g-CN-0.5 mg PTCDA (b), g-CN-1 mg PTCDA (c), g-CN-10 mg PTCDA (d), g-CN-100 mg PTCDA (e), g-CN-1 g PTCDA (f), and PTCDA (g), Figure S3. TEM (a), XRD pattern (b), and FT-IR spectra (c) of g-CN-1 mg PTCDA-Co sample before and after four cycles of catalytic reaction, Table S1. Surface elemental composition of g-CN, g-CN-1 mg PTCDA and g-CN-10 mg PTCDA based on XPS analysis, Table S2. The comparison with other DA structure photocatalysts towards CO<sub>2</sub> reduction under visible light, Table S3. The fitting parameters and average decay time of the time-resolved PL, rate constants of charge separation (k<sub>ET</sub>) and quantum yield ( $\eta_{\text{ET}}$ ) for g-CN and g-CN-1 mg PTCDA, Table S4. The fitting values for the electrochemical impedance spectroscopy simulation fit for g-CN and g-CN-1 mg PTCDA. References [12,15,40,46–49] are cited in the supplementary materials.

**Author Contributions:** S.T. and F.B. conceived the idea. X.C. and J.W. performed the experiments. X.R. provided assistance in data analysis and characterization. All authors have read and agreed to the published version of the manuscript.

**Funding:** This work was financially supported by the National Natural Science Foundation of China (NSFC) U21A2085; Zhongyuan high level talents special support plan 204200510009; Scientific and Technological Innovation Team in University of Henan Province 20IRTSTHN001.

**Conflicts of Interest:** The authors declare no conflict of interest.

## References

1. Xie, Y.; Ou, P.; Wang, X.; Xu, Z.; Li, Y.C.; Wang, Z.; Huang, J.E.; Wicks, J.; McCallum, C.; Wang, N.; et al. High carbon utilization in CO<sub>2</sub> reduction to multi-carbon products in acidic media. *Nat. Catal.* **2022**, *5*, 564–570. [[CrossRef](#)]
2. Xie, S.; Li, Y.; Sheng, B.; Zhang, W.; Wang, W.; Chen, C.; Li, J.; Sheng, H.; Zhao, J. Self-reconstruction of paddle-wheel copper-node to facilitate the photocatalytic CO<sub>2</sub> reduction to ethane. *Appl. Catal. B* **2022**, *310*, 121320. [[CrossRef](#)]
3. Yang, Z.; Yang, J.; Yang, K.; Zhu, X.; Zhong, K.; Zhang, M.; Ji, H.; He, M.; Li, H.; Xu, H. Synergistic Effect in Plasmonic CuAu Alloys as Co-Catalyst on SnIn<sub>4</sub>S<sub>8</sub> for Boosted Solar-Driven CO<sub>2</sub> Reduction. *Catalysts* **2022**, *12*, 1588. [[CrossRef](#)]
4. Li, J.; Zhang, M.; Guan, Z.; Li, Q.; He, C.; Yang, J. Synergistic effect of surface and bulk single-electron-trapped oxygen vacancy of TiO<sub>2</sub> in the photocatalytic reduction of CO<sub>2</sub>. *Appl. Catal. B* **2017**, *206*, 300–307. [[CrossRef](#)]
5. Cui, Y.; Ge, P.; Chen, M.; Xu, L. Research Progress in Semiconductor Materials with Application in the Photocatalytic Reduction of CO<sub>2</sub>. *Catalysts* **2022**, *12*, 372. [[CrossRef](#)]
6. Wang, X.; Blechert, S.; Antonietti, M. Polymeric Graphitic Carbon Nitride for Heterogeneous Photocatalysis. *ACS Catal.* **2012**, *2*, 1596–1606. [[CrossRef](#)]
7. Zheng, J.Y.; Pawar, A.U.; Kang, Y.S. Preparation of C<sub>3</sub>N<sub>4</sub> Thin Films for Photo-/Electrocatalytic CO<sub>2</sub> Reduction to Produce Liquid Hydrocarbons. *Catalysts* **2022**, *12*, 1399. [[CrossRef](#)]
8. Wang, K.; Li, Q.; Liu, B.; Cheng, B.; Ho, W.; Yu, J. Sulfur-doped g-C<sub>3</sub>N<sub>4</sub> with enhanced photocatalytic CO<sub>2</sub>-reduction performance. *Appl. Catal. B* **2015**, *176–177*, 44–52. [[CrossRef](#)]
9. Ong, W.-J.; Tan, L.-L.; Ng, Y.H.; Yong, S.-T.; Chai, S.-P. Graphitic Carbon Nitride (g-C<sub>3</sub>N<sub>4</sub>)-Based Photocatalysts for Artificial Photosynthesis and Environmental Remediation: Are We a Step Closer to Achieving Sustainability? *Chem. Rev.* **2016**, *116*, 7159–7329. [[CrossRef](#)]
10. Ding, J.; Tang, Q.; Fu, Y.; Zhang, Y.; Hu, J.; Li, T.; Zhong, Q.; Fan, M.; Kung, H.H. Core-Shell Covalently Linked Graphitic Carbon Nitride-Melamine-Resorcinol-Formaldehyde Microsphere Polymers for Efficient Photocatalytic CO<sub>2</sub> Reduction to Methanol. *J. Am. Chem. Soc.* **2022**, *144*, 9576–9585. [[CrossRef](#)] [[PubMed](#)]
11. Wu, X.; Li, D.; Huang, Y.; Chen, B.; Luo, B.; Shen, H.; Wang, M.; Yu, T.; Shi, W. Construction of binary donor-acceptor conjugated copolymer in g-C<sub>3</sub>N<sub>4</sub> for enhanced visible light-induced hydrogen evolution. *Appl. Surf. Sci.* **2021**, *565*, 150012. [[CrossRef](#)]
12. Zhang, X.; Song, X.; Yan, Y.; Huo, P. Construction of carbon nitride based intramolecular D-A system for effective photocatalytic reduction of CO<sub>2</sub>. *Catal. Lett.* **2022**, *152*, 559–569. [[CrossRef](#)]
13. Yu, F.; Wang, Z.; Zhang, S.; Wu, W.; Ye, H.; Ding, H.; Gong, X.; Hua, J. Construction of polymeric carbon nitride and dibenzothio-phene dioxide-based intramolecular donor-acceptor conjugated copolymers for photocatalytic H<sub>2</sub> evolution. *Nanoscale Adv.* **2021**, *3*, 1699–1707. [[CrossRef](#)] [[PubMed](#)]
14. Zhang, J.-W.; Pan, L.; Zhang, X.; Shi, C.; Zou, J.-J. Donor-acceptor carbon nitride with electron-withdrawing chlorine group to promote exciton dissociation. *Chin. J. Catal.* **2021**, *42*, 1168–1175. [[CrossRef](#)]
15. Song, X.; Zhang, X.; Wang, M.; Li, X.; Zhu, Z.; Huo, P.; Yan, Y. Fabricating intramolecular donor-acceptor system via covalent bonding of carbazole to carbon nitride for excellent photocatalytic performance towards CO<sub>2</sub> conversion. *J. Colloid Interface Sci.* **2021**, *594*, 550–560. [[CrossRef](#)]
16. Zhu, C.; Wei, T.; Wei, Y.; Wang, L.; Lu, M.; Yuan, Y.; Yin, L.; Huang, L. Unravelling intramolecular charge transfer in donor-acceptor structured g-C<sub>3</sub>N<sub>4</sub> for superior photocatalytic hydrogen evolution. *J. Mater. Chem. A* **2021**, *9*, 1207–1212. [[CrossRef](#)]
17. Song, J.; Chen, Y.; Sun, D.; Li, X. Perylenetetracarboxylic diimide modified Zn<sub>0.7</sub>Cd<sub>0.3</sub>S hybrid photocatalyst for efficient hydrogen production from water under visible light irradiation. *Inorg. Chem. Commun.* **2018**, *92*, 27–34. [[CrossRef](#)]
18. Sun, T.; Song, J.; Jia, J.; Li, X.; Sun, X. Real roles of perylenetetracarboxylic diimide for enhancing photocatalytic H<sub>2</sub>-production. *Nano Energy* **2016**, *26*, 83–89. [[CrossRef](#)]
19. Wei, W.; Zhu, Y. TiO<sub>2</sub>@Perylene Diimide Full-Spectrum Photocatalysts via Semi-Core-Shell Structure. *Small* **2019**, *15*, 1903933. [[CrossRef](#)]
20. Yang, X.; Li, Y.; Chen, G.Y.; Liu, H.R.; Yuan, L.L.; Yang, L.; Liu, D. ZnSnO<sub>3</sub> Quantum Dot/Perylene Diimide Supramolecular Nanorod Heterojunction Photocatalyst for Efficient Phenol Degradation. *ACS Appl. Nano Mater.* **2022**, *5*, 9829–9839. [[CrossRef](#)]
21. Zhang, Z.; Wang, J.; Liu, D.; Luo, W.; Zhang, M.; Jiang, W.; Zhu, Y. Highly Efficient Organic Photocatalyst with Full Visible Light Spectrum through  $\pi$ - $\pi$  Stacking of TCNQ-PTCDI. *ACS Appl. Mater. Interfaces* **2016**, *8*, 30225–30231. [[CrossRef](#)]
22. Wang, X.; Meng, J.; Yang, X.; Hu, A.; Yang, Y.; Guo, Y. Fabrication of a Perylene Tetracarboxylic Diimide-Graphitic Carbon Nitride Heterojunction Photocatalyst for Efficient Degradation of Aqueous Organic Pollutants. *ACS Appl. Mater. Interfaces* **2019**, *11*, 588–602. [[CrossRef](#)]
23. Zhang, J.; Zhao, X.; Wang, Y.; Gong, Y.; Cao, D.; Qiao, M. Peroxymonosulfate-enhanced visible light photocatalytic degradation of bisphenol A by perylene imide-modified g-C<sub>3</sub>N<sub>4</sub>. *Appl. Catal. B* **2018**, *237*, 976–985. [[CrossRef](#)]
24. Xing, C.; Yu, G.; Chen, T.; Liu, S.; Sun, Q.; Liu, Q.; Hu, Y.; Liu, H.; Li, X. Perylenetetracarboxylic diimide covalently bonded with mesoporous g-C<sub>3</sub>N<sub>4</sub> to construct direct Z-scheme heterojunctions for efficient photocatalytic oxidative coupling of amines. *Appl. Catal. B* **2021**, *298*, 120534. [[CrossRef](#)]
25. Wang, Y.; Zhou, J.; Hao, X.; Wang, Y.; Zou, Z. Z-scheme PTCDA/g-C<sub>3</sub>N<sub>4</sub> photocatalyst based on interfacial strong interaction for efficient photooxidation of benzylamine. *Appl. Surf. Sci.* **2018**, *456*, 861–870. [[CrossRef](#)]
26. Yuan, Y.-J.; Shen, Z.-K.; Wang, P.; Li, Z.; Pei, L.; Zhong, J.; Ji, Z.; Yu, Z.-T.; Zou, Z. Metal-free broad-spectrum PTCDA/g-C<sub>3</sub>N<sub>4</sub> Z-scheme photocatalysts for enhanced photocatalytic water oxidation. *Appl. Catal. B* **2020**, *260*, 118179. [[CrossRef](#)]

27. Wang, X.; Maeda, K.; Thomas, A.; Takanabe, K.; Xin, G.; Carlsson, J.M.; Domen, K.; Antonietti, M. A metal-free polymeric photocatalyst for hydrogen production from water under visible light. *Nat. Mater.* **2009**, *8*, 76–80. [[CrossRef](#)]
28. Tian, S.; Chen, S.; Ren, X.; Hu, Y.; Hu, H.; Sun, J.; Bai, F. An efficient visible-light photocatalyst for CO<sub>2</sub> reduction fabricated by cobalt porphyrin and graphitic carbon nitride via covalent bonding. *Nano Res.* **2020**, *13*, 2665–2672. [[CrossRef](#)]
29. Zong, X.; Niu, L.; Jiang, W.; Yu, Y.; An, L.; Qu, D.; Wang, X.; Sun, Z. Constructing creatinine-derived moiety as donor block for carbon nitride photocatalyst with extended absorption and spatial charge separation. *Appl. Catal. B* **2021**, *291*, 120099. [[CrossRef](#)]
30. Xie, Z.; Wang, W.; Ke, X.; Cai, X.; Chen, X.; Wang, S.; Lin, W.; Wang, X. A heptazine-based polymer photocatalyst with donor-acceptor configuration to promote exciton dissociation and charge separation. *Appl. Catal. B* **2023**, *325*, 122312. [[CrossRef](#)]
31. Wang, C.; Wan, Q.; Cheng, J.; Lin, S.; Savateev, A.; Antonietti, M.; Wang, X. Efficient aerobic oxidation of alcohols to esters by acidified carbon nitride photocatalysts. *J. Catal.* **2021**, *393*, 116–125. [[CrossRef](#)]
32. Yu, H.; Shi, R.; Zhao, Y.; Bian, T.; Zhao, Y.; Zhou, C.; Waterhouse, G.I.N.; Wu, L.-Z.; Tung, C.-H.; Zhang, T. Alkali-Assisted Synthesis of Nitrogen Deficient Graphitic Carbon Nitride with Tunable Band Structures for Efficient Visible-Light-Driven Hydrogen Evolution. *Adv. Mater.* **2017**, *29*, 1605148. [[CrossRef](#)] [[PubMed](#)]
33. Chen, Q.; Li, S.; Xu, H.; Wang, G.; Qu, Y.; Zhu, P.; Wang, D. Co-MOF as an electron donor for promoting visible-light photoactivities of g-C<sub>3</sub>N<sub>4</sub> nanosheets for CO<sub>2</sub> reduction. *Chin. J. Catal.* **2020**, *41*, 514–523. [[CrossRef](#)]
34. Fu, J.; Zhu, B.; Jiang, C.; Cheng, B.; You, W.; Yu, J. Hierarchical Porous O-Doped g-C<sub>3</sub>N<sub>4</sub> with Enhanced Photocatalytic CO<sub>2</sub> Reduction Activity. *Small* **2017**, *13*, 1603938. [[CrossRef](#)]
35. Li, Q.; Wang, S.; Sun, Z.; Tang, Q.; Liu, Y.; Wang, L.; Wang, H.; Wu, Z. Enhanced CH<sub>4</sub> selectivity in CO<sub>2</sub> photocatalytic reduction over carbon quantum dots decorated and oxygen doping g-C<sub>3</sub>N<sub>4</sub>. *Nano Res.* **2019**, *12*, 2749–2759. [[CrossRef](#)]
36. Qin, J.; Wang, S.; Ren, H.; Hou, Y.; Wang, X. Photocatalytic reduction of CO<sub>2</sub> by graphitic carbon nitride polymers derived from urea and barbituric acid. *Appl. Catal. B* **2015**, *179*, 1–8. [[CrossRef](#)]
37. Zhang, H.; Wei, J.; Dong, J.; Liu, G.; Shi, L.; An, P.; Zhao, G.; Kong, J.; Wang, X.; Meng, X.; et al. Efficient visible-light-driven carbon dioxide reduction by a single-atom implanted metal-organic framework. *Angew. Chem. Int. Ed.* **2016**, *55*, 14310–14314. [[CrossRef](#)]
38. Wang, S.; Yao, W.; Lin, J.; Ding, Z.; Wang, X. Cobalt Imidazolate Metal-Organic Frameworks Photosplit CO<sub>2</sub> under Mild Reaction Conditions. *Angew. Chem. Int. Ed.* **2014**, *53*, 1034–1038. [[CrossRef](#)]
39. Wang, S.; Lin, J.; Wang, X. Semiconductor-redox catalysis promoted by metal-organic frameworks for CO<sub>2</sub> reduction. *Phys. Chem. Chem. Phys.* **2014**, *16*, 14656–14660. [[CrossRef](#)]
40. Zhang, X.; Wang, M.; Song, X.; Yan, Y.; Huo, P.; Yan, Y.; Yang, B. Boosting charge carrier separation efficiency by constructing an intramolecular DA system towards efficient photoreduction of CO<sub>2</sub>. *New J. Chem.* **2021**, *45*, 6042–6052. [[CrossRef](#)]
41. Fan, X.; Zhang, L.; Cheng, R.; Wang, M.; Li, M.; Zhou, Y.; Shi, J. Construction of Graphitic C<sub>3</sub>N<sub>4</sub>-Based Intramolecular Donor-Acceptor Conjugated Copolymers for Photocatalytic Hydrogen Evolution. *ACS Catal.* **2015**, *5*, 5008–5015. [[CrossRef](#)]
42. Song, X.; Li, X.; Zhang, X.; Wu, Y.; Ma, C.; Huo, P.; Yan, Y. Fabricating C and O co-doped carbon nitride with intramolecular donor-acceptor systems for efficient photoreduction of CO<sub>2</sub> to CO. *Appl. Catal. B* **2020**, *268*, 118736. [[CrossRef](#)]
43. Wei, Y.; Li, X.; Liu, Q.; Zhang, Y.; Zhang, K.; Huo, P.; Yan, Y. Leaf-Vein structure like g-C<sub>3</sub>N<sub>4</sub>/P-MWNTs donor-accepter hybrid catalyst for efficient CO<sub>2</sub> photoreduction. *Carbon* **2022**, *188*, 59–69. [[CrossRef](#)]
44. Qu, D.; Liu, J.; Miao, X.; Han, M.; Zhang, H.; Cui, Z.; Sun, S.; Kang, Z.; Fan, H.; Sun, Z. Peering into water splitting mechanism of g-C<sub>3</sub>N<sub>4</sub>-carbon dots metal-free photocatalyst. *Appl. Catal. B* **2018**, *227*, 418–424. [[CrossRef](#)]
45. Jiang, W.; Zong, X.; An, L.; Hua, S.; Miao, X.; Luan, S.; Wen, Y.; Tao, F.F.; Sun, Z. Consciously Constructing Heterojunction or Direct Z-Scheme Photocatalysts by Regulating Electron Flow Direction. *ACS Catal.* **2018**, *8*, 2209–2217. [[CrossRef](#)]
46. Song, X.; Mao, W.; Wu, Y.; Wang, M.; Liu, X.; Zhou, W.; Huo, P. Fabricating Carbon Nitride-Based 3D/0D Intramolecular Donor-Acceptor Catalysts for Efficient Photoreduction of CO<sub>2</sub>. *New J. Chem.* **2022**, *46*, 20225–20234. [[CrossRef](#)]
47. Hayat, A.; Rahman, M.U.; Khan, I.; Khan, J.; Sohail, M.; Yasmeen, H.; Liu, S.; Qi, K.; Lv, W. Conjugated Electron Donor-Acceptor Hybrid Polymeric Carbon Nitride as a Photocatalyst for CO<sub>2</sub> Reduction. *Molecules* **2019**, *24*, 1779. [[CrossRef](#)] [[PubMed](#)]
48. Zhong, H.; Hong, Z.; Yang, C.; Li, L.; Xu, Y.; Wang, X.; Wang, R. A Covalent Triazine-Based Framework Consisting of Donor-Acceptor Dyads for Visible-Light-Driven Photocatalytic CO<sub>2</sub> Reduction. *ChemSusChem* **2019**, *12*, 4493–4499. [[CrossRef](#)]
49. Xu, N.; Diao, Y.; Qin, X.; Xu, Z.; Ke, H.; Zhu, X. Donor-Acceptor Covalent Organic Frameworks of Nickel (II) Porphyrin for Selective and Efficient CO<sub>2</sub> Reduction into CO. *Dalton Trans.* **2020**, *49*, 15587–15591. [[CrossRef](#)]

**Disclaimer/Publisher's Note:** The statements, opinions and data contained in all publications are solely those of the individual author(s) and contributor(s) and not of MDPI and/or the editor(s). MDPI and/or the editor(s) disclaim responsibility for any injury to people or property resulting from any ideas, methods, instructions or products referred to in the content.